Research Article

Study on the enhancement of photocatalytic environment purification through ubiquitous-red-clay loading

Tetsuya Kako[1] · Fumihiko Ichihara[1,2] · Guigao Liu[1] · Xianguang Meng[1,3] · Jinhua Ye[1,2]

Abstract

Tungsten oxide (WO_3) is regarded as a promising visible-light-sensitive photocatalyst, but its activity is not high. Further enhancement of its activity has been anticipated using techniques such as loading of a cocatalyst to apply the oxide to indoor environmental remediation; Pt has been reported as a good cocatalyst for WO_3 photocatalysis. However, Pt is precious and expensive metal. Thus, in this study, we sought to find a ubiquitous cocatalyst and suitable photocatalyst system. As a result, this study revealed that loading a ubiquitous material of red-clay enhanced WO_3 photocatalytic activity remarkably. As photocatalyst samples, mixtures consisting of the clay and WO_3 with different weight ratios were prepared using a simple kneading method. Their photocatalytic activity was evaluated from decomposition of harmful organic contaminant, 2-propanol into CO_2 under visible-light irradiation. The WO_3 with 10% of the clay loading showed the highest activity among the samples and much higher activity than pure WO_3. This higher activity might derive from the clay's promotion of H_2O_2 decomposition and charge separation (holes and electrons). The H_2O_2 was generated from photocatalytic O_2 reduction. This formation and accumulation on the pure WO_3 surface led to decreased activity.

Keywords TiO_2 · Remediation · Zeolite · Natural mineral · Optical absorption

1 Introduction

The global environment has been polluted by harmful substances of many kinds including volatile organic compounds (VOCs), causing damage to human health. It is extremely important to remove these harmful compounds and to purify the living environment. Purification by photocatalysis is an effective method to decompose harmful airborne organic contaminants [1, 2]. The decomposition mechanism is the following: when light is irradiated on a photocatalyst and the band gap is smaller than the light energy, the photocatalyst absorbs the light. Carriers (electrons and holes) are generated. The holes usually have strong oxidizing capability [3] to mineralize organic compounds, leading to production of much cleaner air.

Anatase-type TiO_2 photocatalyst with low cost has been used for outdoor applications [4–6]. The semiconductor works as a photocatalyst under irradiation of UV light, a minor component of solar light. However, TiO_2 is not useful for indoor applications because TiO_2 can absorb only in the UV region. Furthermore, indoor lighting has very weak UV illumination. Visible-light-sensitive photocatalyst with high activity is promising for indoor air cleaning because indoor lighting can emit intense visible light. Consequently, the development of novel visible-light-sensitive

photocatalysts and low-cost earth-abundant photocatalysts has been anticipated and explored [7–24].

Yellow semiconductor WO_3, with a band gap of 2.6–2.8 eV, is recognized as a promising candidate among visible-light-sensitive photocatalysts. Its potential at the bottom of the conduction band (CB) is more positive than that for one electron oxygen reduction [25]. When WO_3 is used as a photocatalyst, its photogenerated electrons cannot be consumed well. Pure WO_3 is deactivated easily. Research related to loading of cocatalysts such as Pt, PtPb, Cu ion, and NaOH on WO_3 has been undertaken to promote electron consumption and to increase its photocatalytic activity [25–32]. However, Pt is a precious metal that cannot be used sufficiently because of its high cost and likely exhaustion of the Pt resources. Other reported cocatalysts are harmful, or the loading process is complex. A safe and abundant cocatalyst is still needed. Therefore, in this study, we tried to develop a novel mixture photocatalyst consisting of WO_3 and ubiquitous cocatalyst; we also sought a simple method to prepare the mixture.

Apparently, soil is an abundant and ubiquitous material that might be a promising cocatalyst. From results of preliminary investigation, we selected red clay among soils. Results showed that red clay is a suitable cocatalyst. Moreover, red-clay-loaded WO_3 exhibits remarkable photocatalytic activity.

2 Experimental

2.1 Material preparation

Red-clay ball (Akadama soil; Tachikawa Heiwa Nouen Co. Ltd., Japan) preheated to 673 K was used for this study. The clay was crushed using a mortar and pestle to prepare fine particles. The crashed material and WO_3 were mixed with proper mixing ratios using a mortar. Samples were obtained after the mixtures were dried at 343 K for 5 h. The weight ratios for the red clay and WO_3 were, respectively, 1:100, 5:100, 10:100, and 50:100. Furthermore, percentage of loading weight in this study was obtained by dividing cocatalyst weight by WO_3 weight and expressed as the divided amount per one hundred. For example, 1 wt% red clay-loaded WO_3 was the sample with the ratio (1:100).

2.2 Characterization

Samples were characterized using several analytical devices. Crystal structures were measured using an X-ray diffractometer (XRD, X'pert Pro; PANalytical B.V., Netherlands) with Cu Kα radiation. Optical absorption spectra were evaluated using a UV–Vis spectrophotometer (UV-2500PC; Shimadzu Corp., Japan). Reflectance spectra were first measured using $BaSO_4$ as a reference. Then, the obtained data were converted into optical absorption spectra using Kubelka–Munk theory. Surface chemical states of the samples were measured using an X-ray photoelectron spectroscope (XPS, AXIS-HS; Kratos Analytical Ltd., UK) with monochromatic Al Kα radiation. Binding energy in the XPS spectra was calibrated using C 1s peak, of which the binding energy is 284.5 eV. The specific surface area was evaluated at 77 K using a surface analyzer (Gemini 2360; Micromeritics Co., USA) with Brunauer–Emmett–Teller (BET) method. The clay chemical composition was estimated using an inductively coupled plasma optical emission spectroscope (ICP-OES, ICPS-8100; Shimadzu Corp.).

Photocatalytic activity was evaluated at room temperature in a 500-mL cylindrical glass reactor [33]. Photocatalytic decomposition of gaseous 2-propanol (IPA) into CO_2 was selected as a model reaction because IPA is often used as a model of an organic gas in this field [34]. Details of the photocatalytic evaluation procedures were the following: We spread powder photocatalyst with weight of 0.4 g uniformly on a Petri dish with 8.5 cm^2 base area. Then, the dish was set on the center of the base in the reactor. After the inside atmosphere was replaced with pure air, concentrated IPA gas was injected to produce concentrations of IPA in the reactor of about 600–800 ppm. The reactor was kept in the dark until the adsorption–desorption equilibrium state was confirmed. Visible light ($400 < \lambda < 530$ nm) was irradiated using 300 W of Xe lamp equipped with Y-44, B390, HA-30 filters, and a water filter. The IPA concentration was measured using a gas chromatograph (GC-14B; Shimadzu Corp., Japan) with a flame-ionized detector (FID). The CO_2 concentration was estimated using the chromatograph (GC-14B) with FID and a methanizer (TN-1; Shimadzu Corp.). The light intensity of the visible-light irradiation, set to about 1 mW cm^{-2}, was measured using a spectroradiometer (UV-40; Ushio Inc., Japan). Maximum CO_2 evolution rate was evaluated from the rate of zero order reaction [$r = k$ (reaction rate constant), and $C = k\,t$] in the range where CO_2 concentration linearly increased against time.

Reduction of O_2 into H_2O_2 might occur during the photocatalytic IPA oxidation. The H_2O_2 generation on the sample was evaluated qualitatively using dimethylphenanthroline (DMP) method [35]. After the reactor was kept in the dark for 10 min after visible-light irradiation, the sample was washed with distilled water. An aqueous solution possibly containing H_2O_2 can be prepared. Phosphate, DMP, and $CuSO_4$ solutions were added to the aqueous solution. The color turns yellow if the solution contains H_2O_2. Its absorbance at 454 nm in wavelength was measured using UV–Vis to calculate the H_2O_2 amount.

3 Results and discussion

3.1 Crystal structure

Red clay has been used since ancient times for many applications such as bricks and horticulture soils. The red-clay ball (akadama) selected for this study is a volcanic product produced in eastern Japan. The clay is reportedly composed of quartz (SiO_2), diaspore (AlOOH), hematite (Fe_2O_3), and goethite (FeOOH) [36, 37]. The clay components were ascertained using XRD in reference to these data.

Figures S1 and 1 depict XRD patterns of the red clay, WO_3, and the mixture. Results confirmed that the clay consisted mainly of quartz (PDF No. 33-1161). Also, diaspore (PDF No. 5-355), hematite (PDF No. 33-664), and goethite (PDF No. 29-713) might be present in the clay. The XRD data in Fig. 1 imply that the WO_3 was a well crystallized oxide with a monoclinic structure (PDF No. 43-1035) [38]. The XRD pattern of the mixture was similar with that of the WO_3, suggesting that crystal structure of the WO_3 was not changed by the loading.

3.2 Chemical composition

The red clay contains silicon (Si) and metals of many kinds. The atomic ratio in the clay was evaluated using ICP. The evaluated ratios of Si to principal component metals are presented in Table 1. Results show that the clay was composed mainly of Si, Al, and Fe. These metal elements are abundant principal components in the crust of the Earth. Furthermore, these three metal-containing compounds were the main components of the chemical compounds including quartz and diaspore, which were detected using XRD (Figure S1). Accordingly, the ICP data support the XRD results. The clay also contained some alkali (K) and alkali earth (Mg) metals.

3.3 XPS analysis

The red clay mainly contains Si, Al and Fe, as described above. The valence states of Si and Al were expected to be +4 and +3, respectively. Two kinds of valence states of Fe ions such as Fe^{2+}, and Fe^{3+} might exist in the clay. The valence state was assessed carefully using XPS. Figure 2 exhibits the XPS spectra of Fe 2p in the clay and Fe_2O_3, which was used as a reference sample. Two peaks are apparent at the binding energy of 711 eV and 725 eV, respectively, corresponding to Fe $2P_{3/2}$ and Fe $2P_{1/2}$ peaks. Yamashita et al. [39, 40] reported that the peaks centered at 711 eV and 709 eV originated, respectively, from Fe^{3+} and Fe^{2+}. We infer that the clay contained Fe^{3+} ion (Figure S2). This result was also evidenced by the fact that XPS data of Fe_2O_3 resembled those of the clay.

3.4 Optical absorption spectra

The visible-light absorption property was evaluated using UV–Vis spectrophotometry. Figure 3 depicts the optical
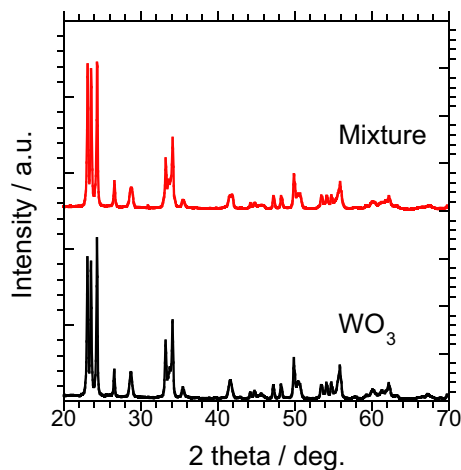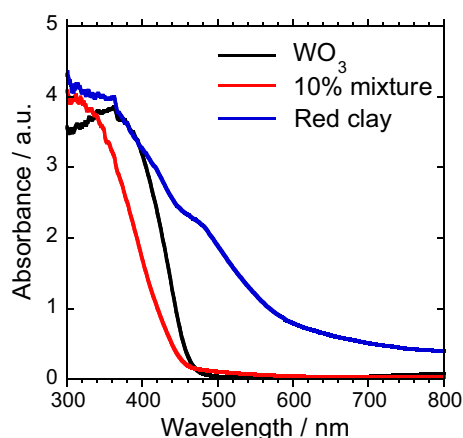

Fig. 1 XRD patterns of WO_3 and a mixture consisting of red clay (10%) and WO_3
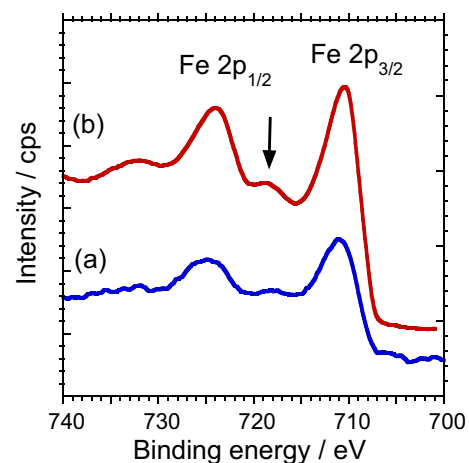
Fig. 2 XPS spectra of **a** red clay and **b** Fe_2O_3. The arrow indicates the satellite peak of Fe $2P_{3/2}$

Table 1 Weight ratios of metals to Si in red-clay ball

	Si	Al	Fe	Mg	Ti	K	Mn
Weight ratio	1	0.62	0.34	0.044	0.020	0.019	3.8×10^{-3}

Fig. 3 Optical absorption spectra of red clay, WO_3, and their mixture (10%)

Fig. 4 Irradiation time dependence of changes of CO_2 generation from IPA decomposition under visible-light irradiation in the presence of WO_3, red clay, and the mixtures: **a** WO_3, **b** 1 wt% of red-clay-loaded WO_3, **c** mixture(clay 5 wt%), **d** mixture (10 wt%), **e** mixture (50 wt%) and **f** red clay

absorption spectra of WO_3, the clay, and the mixtures. WO_3 can absorb light partially in visible light region. Its absorption threshold is about 480 nm. The red clay, which was light brown, can absorb light more widely. Its weak absorption tail extends beyond about 600 nm. Visible-light absorption between 400 and 600 nm might derive dominantly from Fe^{3+}-containing oxides in the clay [41].

The mixture can absorb visible light well, but its onset absorption edge was blue-shifted by 10 nm compared with that of pure WO_3. Similar shifts were observed in other mixtures of NaOH-loaded WO_3 and $NaBiO_3$-loaded WO_3, suggesting that it was not relevant to species of the loaded cocatalysts. Absorption spectra are reported to be affected by many factors including size [42], crystallinity [42], morphology [43], surface functional groups [30, 44], and grain boundary [45]. Because its size, crystallinity, and morphology did not change by mixing, this blue shift might be related mainly to changes in the amounts of surface functional groups [30, 44] and grain boundary of WO_3. The grain boundary may change because of stress from the mixing on a mortar.

3.5 Photocatalytic oxidation property

In photocatalytic oxidation of gaseous IPA, acetone is first generated as an intermediate in the gas phase [33]. Then, acetone is oxidized further into CO_2 via carboxylic acids such as formate (–COOH) and acetic acid (Figure S3) [46]. Organic compounds of many kinds might be generated as intermediates. The final product (CO_2) was monitored carefully for this evaluation of photocatalytic activity.

Figure 4 presents the irradiation time dependence of variation of CO_2 evolution over WO_3 or the mixture under visible-light irradiation. Carbon dioxide was rarely evolved on pure WO_3 with less than 200 h of irradiation. In contrast,
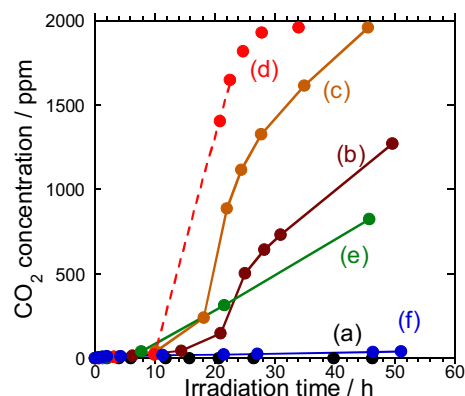
the mixture consisting of WO_3 and the clay (10%) showed remarkable photocatalytic activity. Most of the IPA was oxidized into the final product, CO_2 within 34 h (Fig. 4). The quantitatively estimated maximum rate (zero order reaction rate: about 130 ppm/h, which was calculated from CO_2 concentrations between about 10 h and 23 h) of CO_2 evolution for this sample, which was not affected by diffusion limitation, was much higher than that for pure WO_3 (0.24 ppm/h, calculated from the concentrations between about 110 h and 170 h). Moreover, the mixture (10%) showed over twice higher activity than the reported high-activity photocatalyst Pt-loaded WO_3 [27] (62 ppm/h, calculated from the concentrations between about 11 h and 24 h), as shown in Figure S4. This result means that the photocatalytic activity can be enhanced sufficiently without using expensive chemicals such as those including precious metals.

We investigated the relation between activity and loading amount of the cocatalyst (clay) to ascertain an optimal amount of the clay loading. Figure 5 exhibits the amount of photocatalytic CO_2 evolution for every sample after about 21 h of visible-light irradiation. The photocatalytic activity increased concomitantly with increasing amounts of the clay between 0 and 10 wt% loading. This tendency might be attributed to cocatalyst loading effects, as described in the next section. In contrast, a wider range of the WO_3 surface was covered with the clay. The WO_3 absorbed the irradiated light less when the mixture contained increased loading amounts, especially exceeding approx. 10%. The activity decreased on the mixture loaded by over 10 wt% of the clay with increasing loading amount (Fig. 5). Results show that the highest activity was exhibited by 10 wt% of the clay-loaded WO_3 because of competition between the cocatalyst effect and absorption effect.
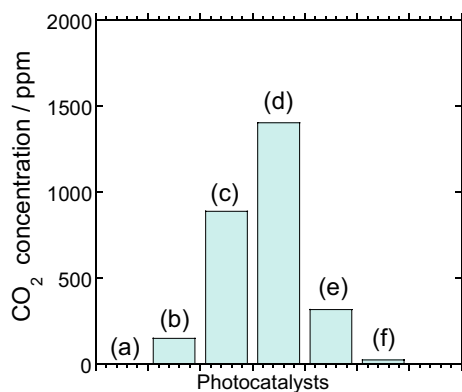
Fig. 5 Amount of CO_2 evolution for photocatalytic IPA decomposition at about 21 h after visible-light radiation: **a** WO_3, **b** 1 wt% of red-clay-loaded WO_3, **c** mixture (5 wt%), **d** mixture (10 wt%), **e** mixture (50 wt%), and **f** red clay

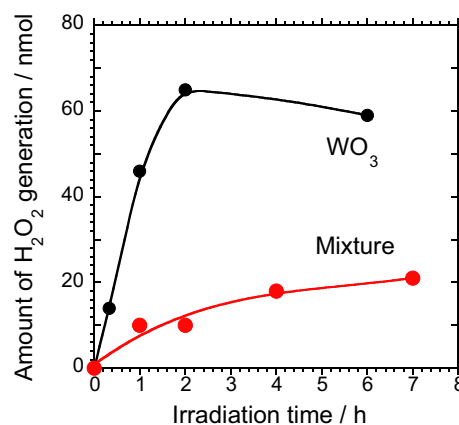**Fig. 6** Effect of irradiation time on H_2O_2 generation for WO_3 and the mixture (10%)

3.6 Mechanism

IPA was oxidized mainly by photogenerated holes. Electrons might contribute importantly to the oxidation. In this section, we specifically examine the role of photogenerated electrons, which were first consumed by reduction of O_2 into H_2O_2 (Reaction (1)) for pure WO_3. The H_2O_2 reportedly decomposed over some time, eventually saturating on the WO_3 surface, leading to deactivation and lower activity of WO_3 [30]. It is crucially important to promote electron consumption, including H_2O_2 decomposition, for the maintenance of WO_3 photocatalytic activity. H^+ in Reaction (1) derived from water adsorbed on the photocatalyst.

$$O_2 + 2H^+ + 2e^- = H_2O_2 \qquad (1)$$

Figure 6 shows that the amount of H_2O_2 formation was measured experimentally on pure WO_3 and the mixture during IPA oxidation. The amount of H_2O_2 first increased gradually and was then saturated on pure WO_3, indicating almost total deactivation within 6 h. However, H_2O_2 on the mixture was generated much less than that on pure WO_3. Photogenerated electrons were consumed using the same reduction process (Reaction (1)), even for the mixture. Therefore, it seems that H_2O_2 was consumed much more quickly on the mixture photocatalyst.

The chemical composition of the clay was checked again to elucidate this superior H_2O_2 consumption property. The clay contained relatively large amounts of highly dispersed Fe^{3+} (Table 1). Apparently, Fe in the clay can play an important role in H_2O_2 consumption. These three reactions (2)–(5) might occur in the consumption process. In reaction (2), part of Fe^{3+} was reduced into Fe^{2+} by photolysis [47]. Furthermore, reaction (3) might occur. Light was absorbed by complexes consisting of Fe^{3+} and carbonic acids (ligand), which
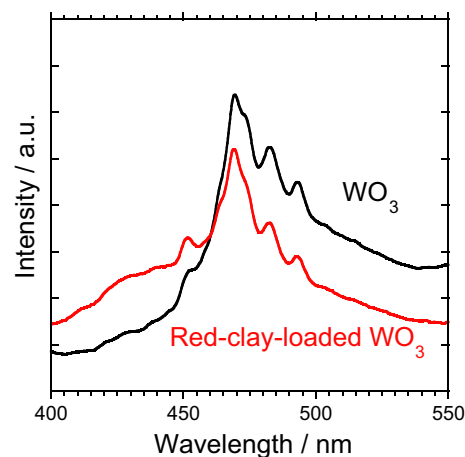
were intermediates in the photocatalytic IPA oxidation; Fe^{3+} was reduced into Fe^{2+} by this light absorption [48]. Except for the above reactions, Fe^{3+} might be directly reduced into
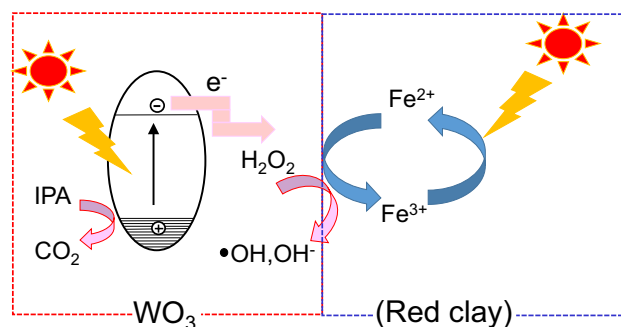
Fig. 7 Schematic illustration of photocatalytic 2-propanol (IPA) oxidation mechanism for red-clay-loaded WO_3
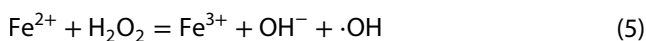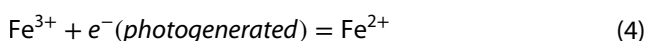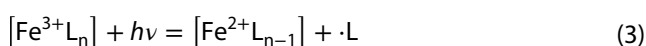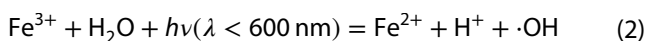

Fig. 8 Photoluminescence (PL) spectra of WO_3 and the mixture (10%) (excitation wavelength: 310 nm)

Table 2 Surface area of the samples

	WO_3	1%	5%	10%	50%	Clay
Surface area (m^2/g)	5.8	7.0	11	12	42	160

Fe^{2+} by photogenerated electrons (Reaction (4)) [49]. These formed Fe^{2+} reacted further with H_2O_2 in reaction (5) (Fenton reaction), resulting in the promotion of H_2O_2 consumption on the mixture [48] (Fig. 7). Radicals of •OH might be generated and be used for IPA decomposition during this H_2O_2 consumption. Consequently, photogenerated electrons can be consumed easily by three reactions. Furthermore, recombination between electrons and holes can decrease, leading to high activity of the mixture.

$$Fe^{3+} + H_2O + h\nu(\lambda < 600\,nm) = Fe^{2+} + H^+ + \cdot OH \quad (2)$$

$$\left[Fe^{3+}L_n\right] + h\nu = \left[Fe^{2+}L_{n-1}\right] + \cdot L \quad (3)$$

$$Fe^{3+} + e^-(photogenerated) = Fe^{2+} \quad (4)$$

$$Fe^{2+} + H_2O_2 = Fe^{3+} + OH^- + \cdot OH \quad (5)$$

Here, L in Eq. (3) represents organic ligands such as $-OCH_3$, $-COOH$, and $-CH_2COOH$.

Photoluminescence (PL) data were measured (Fig. 8) because weaker intensity of PL spectra from band-to-band transition indicates better separation of photogenerated charges (holes and electrons) [50]. The PL spectrum due to band-to-band transition for WO_3 appears at around 450–480 nm of wavelength [51]. The PL intensity around at around 450–480 nm for the clay-loaded WO_3 was weaker than that for pure WO_3, indicating that charge separation was promoted by addition of the clay. This result may be explained as follows: On pure WO_3, photogenerated electrons were consumed by oxygen reduction into H_2O_2. However, H_2O_2 was accumulated gradually on the WO_3 surface, leading to suppress of H_2O_2 formation and electron consumption. On the other hand, on the red-clay-loaded WO_3, H_2O_2 was decomposed by Fe^{2+}, leading to less inhibition of further O_2 reduction (H_2O_2 formation) and electron consumption. As a result, recombination between electrons and holes was more difficult to occur on the mixture.

To confirm the Fe effect further, photocatalytic activity for 5 wt% of Fe^{3+}-doped, zeolite-loaded WO_3 was evaluated (Figure S4). The activity for the Fe-doped-zeolite-loaded WO_3 also showed relatively high activity. These results showed that loading of a Fe^{3+}-containing compound gave a positive effect for WO_3 photocatalysis.

We examined the effects of high surface area for the cocatalyst because a larger surface area often positively affects photocatalytic activity. The BET surface areas are presented in Table 2. The surface areas of the WO_3 and

the mixture (10% of cocatalyst loading) were estimated, respectively, as 5.8 and 12 m^2/g. The area of the mixture was about twice that of the WO_3, which suggests that high surface area of the cocatalyst also contributed to the high photocatalytic activity of the mixtures. However, the effect of larger surface area on the activity's difference is very limited (Figure S5) because the surface area was just twice higher.

4 Conclusion

Mixtures of WO_3 and red clay were prepared using a simple kneading method. The samples absorbed visible light well and showed photocatalytic activity under visible-light irradiation. The photocatalytic activity was evaluated from IPA decomposition into CO_2. Relation between photocatalytic activity and mixing ratios (red clay to WO_3) exhibited that 10 wt% of red-clay-loaded WO_3 showed the highest activity. Furthermore, the activity of the mixture was higher than that of Pt-loaded WO_3 with relatively high activity. This higher activity of the mixture should derive from good H_2O_2 consumption efficiency of the red clay. H_2O_2 that was generated from photocatalytic reduction of O_2 on WO_3 might accumulate on the WO_3 surface and suppress WO_3 photocatalytic activity.

Salient benefits of this mixture photocatalyst are its high activity and its usage of ubiquitous red clay as a cocatalyst. The clay is remarkably cheap and abundant. The mixture photocatalysts and preparation process are eco-friendly because no wastes, even wastewater, are produced during its preparation.

Compliance with ethical standards

Conflict of interest The manuscript does not contain conflict of interest.

References

1. Hashimoto K, Irie H, Fujishima A (2005) TiO_2 photocatalysis: a historical overview and future prospects. Jpn J Appl Phys 44:8269–8285

2. Peral J, Ollis DF (1992) Heterogeneous photocatalytic oxidation of gas-phase organics for air purification—acetone, 1-butanol, butyraldehyde, formaldehyde, and meta-xylene oxidation. J Catal 136:554–565

3. Konstantinou KI, Albanis TA (2004) TiO_2-assisted photocatalytic degradation of azo dyes in aqueous solution: kinetic and mechanistic investigations: a review. Appl Catal B Environ 49:1–14

4. Fujishima A, Zhang XT (2006) Titanium dioxide photocatalysis: present situation and future approaches. C R Chim 9:750–760

5. Hoffmann MR, Martin ST, Choi WY, Bahnemann DW (1995) Environmental applications of semiconductor photocatalysis. Chem Rev 95:69–96

6. Mills A, LeHunte S (1997) An overview of semiconductor photocatalysis. J Photochem Photobiol A Chem 108:1–35

7. Wang XC, Maeda K, Thomas A, Takanabe K, Xin G, Cartsson JM, Domen K, Antonietti M (2009) A metal-free polymeric photocatalyst for hydrogen production from water under visible light. Nat Mater 8:76–80

8. Kim HG, Hwang DW, Lee JS (2004) An undoped, single-phase oxide photocatalyst working under visible light. J Am Chem Soc 126:8912–8913

9. Ouyang SX, Ye JH (2011) Beta-$AgAl_{1-x}Ga_xO_2$ solid-solution photocatalysts: continuous modulation of electronic structure toward high-performance visible-light photoactivity. J Am Chem Soc 133:7757–7763

10. Yan SC, Li Z, Zou Z (2009) Photodegradation performance of g-C_3N_4 fabricated by directly heating melamine. Langmuir 25:10397–10401

11. Kako T, Umezawa N, Xie K, Ye JH (2013) Undoped visible-light-sensitive titania photocatalyst. J Mater Sci 48:108–114

12. Wang DF, Kako T, Ye JH (2008) Efficient photocatalytic decomposition of acetaldehyde over a solid-solution perovskite $(Ag_{0.75}Sr_{0.25})(Nb_{0.75}Ti_{0.25})O_3$ under visible-light irradiation. J Am Chem Soc 130:2724–2725

13. Li Z, Zhang QW, Liu XZ, Wu L, Hu HM, Zhao Y (2018) One-step mechanochemical synthesis of plasmonic Ag/Zn-Al LDH with excellent photocatalytic activity. J Mater Sci 53:12795–12806

14. Xu JJ, Chen YF, Dong ZY, Wang QK, Yue ST, Huang H (2018) Facile synthesis of the Ti^{3+}-TiO_2-rGO compound with controllable visible light photocatalytic performance: GO regulating lattice defects. J Mater Sci 53:12770–12780

15. Kako T, Zou ZG, Katagiri M, Ye JH (2007) Decomposition of organic compounds over $NaBiO_3$ under visible light irradiation. Chem Mater 19:198–202

16. Yi ZG, Ye JH, Kikugawa N, Kako T, Ouyang SX, Stuart-Williams H, Yang H, Cao JY, Luo WJ, Li Z, Liu Y, Withers RL (2010) An orthophosphate semiconductor with photooxidation properties under visible-light irradiation. Nat Mater 9:559–564

17. Kako T, Ye J (2010) Synergistic effect of different phase on the photocatalytic activity of visible light sensitive silver antimonates. J Mol Catal A Chem 320:79–84

18. Asahi R, Morikawa T, Ohwaki T, Aoki K, Taga Y (2001) Visible-light photocatalysis in nitrogen-doped titanium oxides. Science 293:269–271

19. Chen YM, Lu AH, Li Y, Zhang LS, Yip HY, Zhao HJ, An TC, Wong PK (2011) Naturally occurring sphalerite as a novel cost-effective photocatalyst for bacterial disinfection under visible light. Environ Sci Technol 45:5689–5695

20. Xia DH, Shen ZR, Huang GC, Wang WJ, Yu JC, Wong PK (2015) Red phosphorus: an earth-abundant elemental photocatalyst for "green" bacterial inactivation under visible light. Environ Sci Technol 49:6264–6273

21. Huang YB, Liang J, Wang XS, Cao R (2017) Multifunctional metal-organic framework catalysts: synergistic catalysis and tandem reactions. Chem Soc Rev 46:126–157

22. Wang WJ, An TC, Li GY, Xia DH, Zhao HJ, Yu JC, Wong PK (2017) Earth-abundant Ni_2P/g-C_3N_4 lamellar nanohybrids for enhanced photocatalytic hydrogen evolution and bacterial inactivation under visible light irradiation. Appl Catal B Environ 217:570–580

23. Hao Q, Wang CX, Huang H, Li W, Du DY, Han D, Qiu T, Chu PK (2015) Aluminum plasmonic photocatalysis. Sci Rep 5:15288

24. Wang WJ, Li GY, Xia DH, An TC, Zhao HJ, Wong PK (2017) Photocatalytic nanomaterials for solar-driven bacterial inactivation: recent progress and challenges. Environ Sci Nano 4:782–799

25. Kako T, Meng X, Ye JH (2015) Solid-base loaded WO_3 photocatalyst for decomposition of harmful organics under visible light irradiation. APL Mater 3:104411

26. Arai T, Horiguchi M, Yanagida M, Gunji T, Sugihara H, Sayama K (2008) Complete oxidation of acetaldehyde and toluene over a Pd/WO_3 photocatalyst under fluorescent- or visible-light irradiation. Chem Commun 43:5565–5567

27. Abe R, Takami H, Murakami N, Ohtani B (2008) Pristine simple oxides as visible light driven photocatalysts: highly efficient decomposition of organic compounds over platinum-loaded tungsten oxide. J Am Chem Soc 130:7780–7781

28. Gunji T, Tsuda T, Jeevagan AJ, Hashimoto M, Tanabe T, Kaneko S, Miyauchi M, Saravanan G, Abe H, Matsumoto F (2014) Visible light induced decomposition of organic compounds on WO_3 loaded PtPb co-catalysts. Catal Commun 56:96–100

29. Irie H, Miura S, Kamiya K, Hashimoto K (2008) Efficient visible light-sensitive photocatalysts: grafting Cu(II) ions onto TiO_2 and WO_3 photocatalysts. Chem Phys Lett 457:202–205

30. Kako T, Meng X, Ye JH (2014) Enhancement of photocatalytic activity for WO_3 by simple NaOH loading. Appl Catal A Gen 488:183–188

31. Katsumata K, Motoyoshi R, Matsushita N, Okada K (2013) Preparation of graphitic carbon nitride g-C_3N_4/WO_3 composites and enhanced visible-light-driven photodegradation of acetaldehyde gas. J Hazard Mater 260:475–482

32. Mizutani M, Isobe T, Matsushita S, Nakajima A (2017) Preparation of visible light photocatalyst by interface reaction between tungsten-molybdenum oxide and copper clusters. Mater Lett 186:135–137

33. Ohko Y, Hashimoto K, Fujishima A (1997) Kinetics of photocatalytic reactions under extremely low-intensity UV illumination on titanium dioxide thin films. J Phys Chem A 101:8057–8062

34. Kako T, Kikugawa N, Ye JH (2008) Photocatalytic activities of $AgSbO_3$ under visible light irradiation. Catal Today 131:197–202

35. Kosaka K, Yamada H, Matsui S, Echigo S, Shishida K (1998) Comparison among the methods for hydrogen peroxide measurements to evaluate advanced oxidation processes: application of a spectrophotometric method using copper(II) ion and 2.9 dimethyl-1,10-phenanthroline. Environ Sci Technol 32:3821–3824

36. Chen RZ, Lei ZF, Yang SJ, Zhang ZY, Yang YN, Sugiura N (2012) Characterization and modification of porous ceramic sorbent for arsenate removal. Colloids Surf A 414:393–399

37. Zhao YX, Yang SJ, Ding D, Chen J, Yang YN, Lei ZF, Feng CP, Zhang ZY (2013) Effective adsorption of Cr(VI) from aqueous solution using natural Akadama clay. J Colloid Interface Sci 395:198–204

38. Zhao C, Yang Y, Zhang Z (2012) Photocatalytic treatment of microcystin-LR-containing wastewater using Pt/WO_3 nanoparticles under simulated solar light. Open J Appl Sci 2:86–92

39. Li P, Jiang EY, Bai HL (2011) Fabrication of ultrathin epitaxial gamma-Fe_2O_3 films by reactive sputtering. J Phys D Appl Phys 44:075003

40. Yamashita T, Hayes P (2008) Analysis of XPS spectra of Fe^{2+} and Fe^{3+} ions in oxide materials. Appl Surf Sci 254:2441–2449

41. Cao JY, Kako T, Kikugawa N, Ye JH (2010) Photoanodic properties of pulsed-laser-deposited alpha-Fe_2O_3 electrode. J Phys D Appl Phys 43:325101

42. Bao DH, Yao X, Wakiya N, Shinozaki K, Mizutani N (2001) Band-gap energies of sol–gel-derived $SrTiO_3$ thin films. Appl Phys Lett 79:3767–3769

43. Song HB, Peng TY, Cai P, Yi HB, Yan CH (2007) Hydrothermal synthesis of flaky crystallized $La_2Ti_2O_7$ for producing hydrogen from photocatalytic water splitting. Catal Lett 113:54–58

44. Li G, Kako T, Ye JH (2008) Synthesis and enhanced photocatalytic activity of $NaNbO_3$ prepared by hydrothermal and polymerized complex methods. J Phys Chem Solid 69:2487–2491

45. Bao BH, Gu HS, Kuang AX (1998) Sol–gel-derived c-axis oriented ZnO thin films. Thin Solid Films 312:37–39

46. Xu WZ, Raftery D (2001) In situ solid-state nuclear magnetic resonance studies of acetone photocatalytic oxidation on titanium oxide surfaces. J Catal 204:110–117

47. Fallmann H, Krutzler T, Bauer R, Malato S, Blanco J (1999) Applicability of the photo-fenton method for treating water containing pesticides. Catal Today 54:309–319

48. Kitsiou V, Filippidis N, Mantzavinos D, Poulios I (2009) Heterogeneous and homogeneous photocatalytic degradation of the insecticide imidacloprid in aqueous solutions. Appl Catal B Environ 86:27–35

49. Sayama K, Yoshida R, Kusama H, Okabe K, Abe Y, Arakawa H (1997) Photocatalytic decomposition of water into H_2 and O_2 by a two-step photoexcitation reaction using a WO_3 suspension catalyst and Fe^{3+}/Fe^{2+} redox system. Chem Phys Lett 277:387–391

50. Huang AL, Xu H, Li Y, Li H, Cheng X, Xia J, Xu Y, Cai G (2013) Visible-light-induced WO_3/g-C_3N_4 composites with enhanced photocatalytic activity. Dalton Trans 42:8606–8616

51. Luo J, Zhao F, Gong L, Chen H, Zhou J, Li Z, Deng S, Xu N (2007) Ultraviolet-visible emission from three-dimensional WO_{3-x} nanowire networks. Appl Phys Lett 91:093124